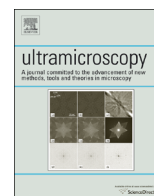




ELSEVIER

Contents lists available at ScienceDirect

## Ultramicroscopy

journal homepage: [www.elsevier.com/locate/ultramic](http://www.elsevier.com/locate/ultramic)

Full length article

# Quantitative measurement of mean inner potential and specimen thickness from high-resolution off-axis electron holograms of ultra-thin layered WSe<sub>2</sub>



Florian Winkler<sup>a,b,\*</sup>, Amir H. Tavabi<sup>a,b</sup>, Juri Barthel<sup>a,c</sup>, Martial Duchamp<sup>a,b</sup>,  
Emrah Yucelen<sup>d</sup>, Sven Borghardt<sup>e</sup>, Beata E. Kardynal<sup>e</sup>, Rafal E. Dunin-Borkowski<sup>a,b</sup>

<sup>a</sup> Ernst Ruska-Centre for Microscopy and Spectroscopy with Electrons (ER-C), Forschungszentrum Jülich, D-52425 Jülich, Germany

<sup>b</sup> Peter Grünberg Institute 5 (PGI-5), Forschungszentrum Jülich, D-52425 Jülich, Germany

<sup>c</sup> Gemeinschaftslabor für Elektronenmikroskopie (GFE), RWTH Aachen University, D-52074 Aachen, Germany

<sup>d</sup> FEI Company, Achtseweg Noord 5, Eindhoven 5600 KA, The Netherlands

<sup>e</sup> Peter Grünberg Institute 9 (PGI-9), Forschungszentrum Jülich, D-52425 Jülich, Germany

## ARTICLE INFO

## Article history:

Received 15 March 2016

Received in revised form

27 July 2016

Accepted 29 July 2016

Available online 30 July 2016

## Keywords:

Transmission electron microscopy

Off-axis electron holography

Mean inner potential

Specimen thickness

Transition metal dichalcogenide

WSe<sub>2</sub>

## ABSTRACT

The phase and amplitude of the electron wavefunction that has passed through ultra-thin flakes of WSe<sub>2</sub> is measured from high-resolution off-axis electron holograms. Both the experimental measurements and corresponding computer simulations are used to show that, as a result of dynamical diffraction, the spatially averaged phase does not increase linearly with specimen thickness close to an [001] zone axis orientation even when the specimen has a thickness of only a few layers. It is then not possible to infer the local specimen thickness of the WSe<sub>2</sub> from either the phase or the amplitude alone. Instead, we show that the combined analysis of phase and amplitude from experimental measurements and simulations allows an accurate determination of the local specimen thickness. The relationship between phase and projected potential is shown to be approximately linear for extremely thin specimens that are tilted by several degrees in certain directions from the [001] zone axis. A knowledge of the specimen thickness then allows the electrostatic potential to be determined from the measured phase. By using this combined approach, we determine a value for the mean inner potential of WSe<sub>2</sub> of  $18.9 \pm 0.8$  V, which is 12% lower than the value calculated from neutral atom scattering factors.

© 2016 The Authors. Published by Elsevier B.V. This is an open access article under the CC BY license (<http://creativecommons.org/licenses/by/4.0/>).

## 1. Introduction

Interest in two-dimensional transition metal dichalcogenide (TMD) materials has increased dramatically in recent years as a result of their potential applications [1–3]. In contrast to graphene, monolayer TMD compounds with the formula MX<sub>2</sub> (M: Mo, W; X: S, Se) have direct bandgaps that lie in the visible range [4]. In these materials, the heavy transition metal atoms lead to strong spin-orbit interactions, resulting in spin-valley splitting in the valence and conduction bands and paving the way for spintronic applications [5,6]. On the one hand, the electronic and optical properties of TMDs depend on the number of layers, i.e., on the thickness of the material. On the other hand, these properties also change depending on the local structure and chemistry of the material,

including the presence of dopants, defects, interfaces with other materials and contamination layers. A deep understanding of the relationship between morphology, structure and chemistry of TMDs and their electronic and optical properties is therefore important for the development of new devices. The ability to measure the local electrostatic potential and specimen thickness of such two-dimensional materials would constitute a substantial contribution to the field.

Off-axis electron holography is a powerful technique for the direct measurement of electrostatic potentials in materials with close to atomic spatial resolution in the transmission electron microscope (TEM) [7–9]. The superposition of an object wave and a reference wave results in the formation of an interference pattern in the image plane, which can be described using the expression

$$I_{\text{hol}}(\mathbf{r}) = 1 + A^2(\mathbf{r}) + 2\rho_c A(\mathbf{r}) \cos(2\pi\mathbf{q}_c \cdot \mathbf{r} + \phi(\mathbf{r})), \quad (1)$$

where  $A$  and  $\phi$  are the amplitude and phase of the object wave,  $\rho_c$

\* Corresponding author at: Ernst Ruska-Center for Microscopy and Spectroscopy with Electrons (ER-C), Forschungszentrum Jülich, D-52425 Jülich, Germany.

E-mail address: [f.winkler@fz-juelich.de](mailto:f.winkler@fz-juelich.de) (F. Winkler).

is the contrast of the hologram fringes, the vector  $\mathbf{r} = (x, y)$  is in the object exit plane and  $\mathbf{q}_c$  describes the tilt of the reference wave with respect to the object wave [10]. In Eq. (1), the first two terms are associated with the centerband in the Fourier transform of the hologram, whereas the third term is associated with the sidebands, from either of which the object wavefunction  $\psi = A\exp(i\phi)$  can be recovered.

For a non-magnetic material, in the absence of dynamical diffraction the phase recorded using off-axis electron holography can be written in the form

$$\phi(x, y) = C_E \int V(x, y, z) dz, \quad (2)$$

where the incident electron beam direction is along  $z$ ,  $V(x, y, z)$  is the local electrostatic potential within (and around) the specimen and  $C_E$  is a constant that depends on the accelerating voltage of the microscope [11]. In the absence of external electric fields, if the specimen is homogeneous along  $z$ , the phase therefore depends linearly on the local specimen thickness  $t(x, y)$  according to the expression

$$\phi(x, y) = C_E V_p(x, y) t(x, y), \quad (3)$$

where  $V_p$  is the projected potential along  $z$ . The amplitude  $A$  is related to the specimen thickness according to a Lambert-Beer law

$$A(x, y) = \exp\left(-\frac{t(x, y)}{2\lambda_{tot}(x, y)}\right), \quad (4)$$

where  $\lambda_{tot}$  is the total mean free path for absorption of electrons due to inelastic and elastic scattering [12].

In practice, the relationships described in Eqs. (2)–(4) are influenced by the fact that the interaction between a high-energy electron and a material is relatively strong when compared, for example, to that in X-ray or neutron scattering. A strong interaction is beneficial on the one hand, as it provides a strong signal for high-precision and high-resolution measurements. On the other hand, electron diffraction then often has to be treated within the dynamical diffraction theory. Enhanced dynamical effects can be expected in general with increasing specimen thickness, higher atomic number, larger electron wavelength and when the incident electron beam direction is along a low-order zone axis of the crystal. Under such conditions, Eqs. (2)–(4) are no longer valid. For example, Lubk et al. showed that dynamical effects are inevitable in electron holographic tomography of GaAs/AlGaAs core-shell nanowires and care has to be taken when interpreting a measured phase in terms of electrostatic potential [13]. Even if there is a linear relationship between phase and specimen thickness, the proportionality factor does not necessarily correspond exactly to the electrostatic potential. Discrepancies may, for example, originate from excitation errors that depend on the orientation of the crystal with respect to the electron beam direction. The interpretation and quantitative analysis of a measurement of phase or amplitude should therefore always ideally be supported by computer simulations.

Here, we study ultra-thin flakes of WSe<sub>2</sub> that have the 2H crystallographic phase. This material has a layered crystallographic structure similar to that of graphite, but with each layer formed by three atomic layers that comprise a central W layer sandwiched by two Se layers, as shown in Fig. 1. The atoms within each WSe<sub>2</sub> layer form strong covalent bonds, whereas van der Waals forces act between adjacent layers. In order to reduce knock-on damage, we use a relatively low electron energy of 80 keV for off-axis electron holography [16]. However, the low accelerating voltage enhances the influence of dynamical diffraction, which is already strong as a result of the relatively high atomic numbers of W ( $Z = 74$ ) and Se ( $Z = 34$ ). We investigate the limitations of the

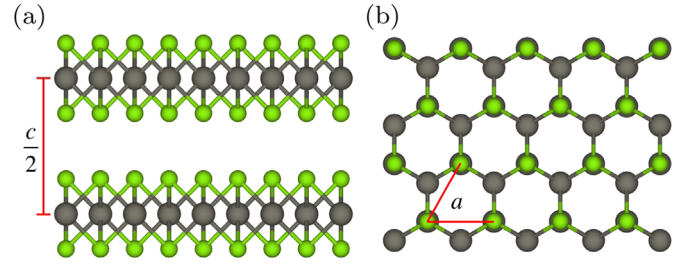


**Fig. 1.** Crystallographic structure of 2H-WSe<sub>2</sub> with the lattice parameters  $a = 3.28 \text{ \AA}$  and  $c = 12.96 \text{ \AA}$  [14]. Green spheres represent Se atoms, while gray spheres represent W atoms. (a) View of the WSe<sub>2</sub> lattice along  $[-120]$ , illustrating its layered structure. (b) View of the WSe<sub>2</sub> lattice along  $[001]$ . The crystal structures are visualized using Vesta software [15]. (For interpretation of the references to color in this figure legend, the reader is referred to the web version of this article.)

linear relationships between both  $\phi$  and  $-\ln(A)$  and specimen thickness according to Eqs. (3) and (4), by performing a quantitative evaluation of experimental electron holograms recorded from specimens of different thickness for varying specimen tilt angles from the  $[001]$  zone axis orientation. The effects of dynamical diffraction are considered by comparing calculations with the experimental measurements. We measure the local specimen thickness and the mean inner potential of WSe<sub>2</sub> despite the presence of strong dynamical effects, thereby also establishing a procedure that can be used for the reliable measurement of electrostatic potentials in devices based on TMDs in future in situ experiments.

## 2. Theory and methods

### 2.1. Mean inner potential

The mean inner potential  $V_0$  is a material-dependent quantity that is defined as the volume average of the atomic electrostatic potentials in a specimen. Accordingly,  $V_0$  depends on the local composition, density and ionicity of the specimen [17,18]. In off-axis electron holography, the local specimen thickness is often determined from measured phases using Eq. (3) if the mean inner potential of the specimen is known.

If a material is considered as an array of neutral atoms, then its mean inner potential can be calculated from electron scattering factors, resulting in a predicted value of  $V_0 = 21.5 \text{ V}$  for WSe<sub>2</sub> [19]. This prediction is expected to overestimate the true value of  $V_0$  by approximately 5–10%, as it neglects the redistribution of electrons due to bonding in solid state materials [11,20].

The quantity measured from the phase, as extracted from an experimental electron hologram, is the projected potential  $V_p$ . Averaging  $V_p$  over the area  $\Omega$  of a projected unit cell under ideal conditions yields the mean inner potential

$$V_0 = \frac{1}{\Omega} \int_{\Omega} V_p(x, y) d\Omega. \quad (5)$$

For a real sample,  $V_0$  is also sensitive to the presence of reconstructions, adsorbates and the redistribution of charge on specimen surfaces [21,22]. Recently, for example, density functional theory (DFT) simulations have been used to show that in III–V semiconductors  $V_0$  depends on the presence and nature of surface adsorbates [23].

### 2.2. Specimen preparation

Specimens of two-dimensional ultra-thin WSe<sub>2</sub> were prepared for off-axis electron holography by transferring flakes of the material onto holey SiN membranes. Before transfer of the flakes, the

membranes were coated with Au on both sides to reduce the effects of electron beam induced charging during examination in the TEM. A light-optical micrograph and a low magnification bright-field TEM image of a successfully transferred WSe<sub>2</sub> flake are shown in Fig. 2.

Flakes were transferred onto the SiN membranes by an all-dry technique similar to that described by Castellanos-Gomez et al. [24]. Briefly, a small WSe<sub>2</sub> crystal was cleaved using polydimethylsiloxane (PDMS) elastomeric films supported on glass slides. After several cleaving steps, thin flakes on these films were identified using light-optical microscopy in transmission mode. A micromanipulation stage was used to align a chosen flake on the PDMS/glass stack to the holey SiN membrane. The flake could be positioned on a partly covered hole in order to provide a vacuum reference wave for off-axis electron holography. When the flake and the PDMS were in contact with the membrane, the glass/PDMS stack was released, leaving the flake on the membrane. Each specimen was annealed in a vacuum furnace overnight at 85 °C, in order to remove residual C-based contamination from its surface, before being inserted into the TEM.

### 2.3. Off-axis electron holography

Off-axis electron holograms of the WSe<sub>2</sub> flakes were recorded on an FEI Titan 50–300 G<sup>3</sup> TEM (FEI Company, NL) operated at an accelerating voltage of 80 kV on a 4096 × 4096 pixel charge-coupled-device camera [25]. As mentioned above, the low accelerating voltage was used to reduce knock-on damage to the specimen. By means of hardware correction of spherical aberration ( $C_s$ ) and chromatic aberration ( $C_c$ ), the spatial resolution of the microscope is extended to 80 pm at 80 kV. The  $C_s/C_c$ -corrector was tuned to obtain a small total  $C_s$  of 10 μm and a  $C_c$  of below 5 μm, with all other axial aberrations up to 4th order being sufficiently small. Off-axial aberrations were corrected up to 3rd order.

Off-axis electron holograms were recorded without using an objective aperture. The biprism voltage was set to 230 V, resulting in a holographic interference fringe spacing of 33 pm with an average fringe contrast of 25% for images recorded at a magnification of 3.5 million. Exposure times for the individual holograms were between 5 and 12 s, corresponding to mean counts of 70–180 electrons per pixel. Vacuum reference electron holograms were acquired after each hologram of the specimen in order to correct for the influence of the imaging and recording system of the microscope [26]. A small underfocus was applied, thereby minimizing the amplitude modulation of the holographic fringes and leading to minimum phase noise, as proposed by Linck [27].

### 2.4. Image processing and analysis

The experimental electron holograms were reconstructed using HoloWorks 5.0 in Digital Micrograph (Gatan Inc., USA). A circular

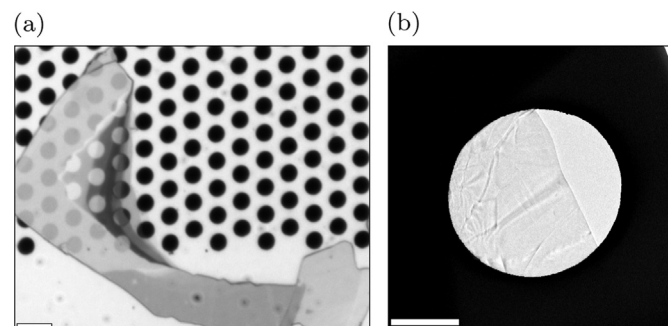


**Fig. 2.** (a) Light-optical micrograph and (b) low magnification TEM image of a WSe<sub>2</sub> flake transferred onto a Au-coated holey SiN membrane. The holes in the SiN membrane are 2.5 μm in diameter. The scale bars are (a) 5 μm and (b) 1 μm.

mask was applied to the sideband in Fourier space, fully transferring all beams up to a diffraction angle of 15 mrad, including the first order diffraction spots of WSe<sub>2</sub> at 14.7 mrad. The mask decays smoothly at its edge between 15 and 17 mrad. Consequently, the final phase and amplitude images have a spatial resolution of 2.8 Å. The choice of this aperture size serves two purposes: (i) to reduce the influence of residual aberrations on the phase and (ii) to use the lattice periodicity to partition the image into projected unit cells, within which mean phases and amplitudes can be calculated. The use of a larger aperture would have no influence on the mean values of the phases and amplitudes in these cells, but could introduce distortions due to aberrations. In order to compensate for a possible linear gradient in the phase, a two-dimensional phase gradient was fitted to the vacuum area and subtracted from each total phase image. Before analysis, the average phase in vacuum was subtracted from each image. Similarly, all amplitude images were normalized by dividing them by the average value measured in vacuum outside the specimen edge.

In order to analyze the spatially averaged phase and amplitude of the WSe<sub>2</sub> lattice, the electron wavefunction was partitioned into regions of unit cell size by means of Voronoi tessellation [28]. The Voronoi cells were positioned with their centers at the positions of local minima in the phase image (yellow crosses in Fig. 3) and applied as a mask to the measured complex electron wavefunction. Hence, each cell is associated with one local minimum in the phase image and consists of all pixels that are closer to this minimum than to any other one. The Voronoi cells correspond to unit cells of WSe<sub>2</sub> and reflect the hexagonal symmetry of the lattice. The average complex number in each cell was calculated and every pixel was set to the average complex number of its corresponding Voronoi cell of area  $\Omega$ , analogous to Eq. (5).

In the presence of defects, lattice distortions, noise or optical aberrations, the shapes of the fitted Voronoi cells may deviate from perfect hexagons. Voronoi cells that deviated strongly in shape and size from perfect hexagons were neglected during further analysis. In order to ensure that Voronoi cells corresponded to complete unit cells, the border of each image was excluded from analysis, the cell size was limited to a specific range and the number of vertices was fixed to six in the tessellation procedure.

### 2.5. Simulations

Multislice calculations were used to simulate the effect of dynamical electron diffraction by means of the Dr. Probe software package [29,30]. The results of the calculations were electron wavefunctions at the exit plane of the specimen.

In the simulations, the WSe<sub>2</sub> structure model was partitioned along the projection direction into 8 equidistant sub-slices of thickness 0.162 nm, such that each slice contained at most one atomic plane. The unit cell of WSe<sub>2</sub> contains two WSe<sub>2</sub> layers in the  $c$ -direction [14]. Accordingly, 6 of the 8 slices contained atoms and 2 empty slices represented empty space between the two layers. Thermal vibrations at room temperature were considered by applying Debye–Waller factors to the elastic electron scattering potential with effective thermal displacement parameters  $B(W) = 0.33 \text{ \AA}^2$  and  $B(\text{Se}) = 0.27 \text{ \AA}^2$  in the projected plane of the 2H-WSe<sub>2</sub> structure [31]. Elastic and absorptive electron scattering potentials were taken from the tables of Weickenmeier and Kohl [32].

Electron wavefunctions were calculated at 80 kV for specimen thicknesses of between 1 and 6 WSe<sub>2</sub> layers. The specimen orientation with respect to the electron beam direction was varied between 0° and 5° from the [001] zone axis towards the [100] crystallographic axis.

Several electron-optical properties of the microscope and image processing parameters have an influence on the electron

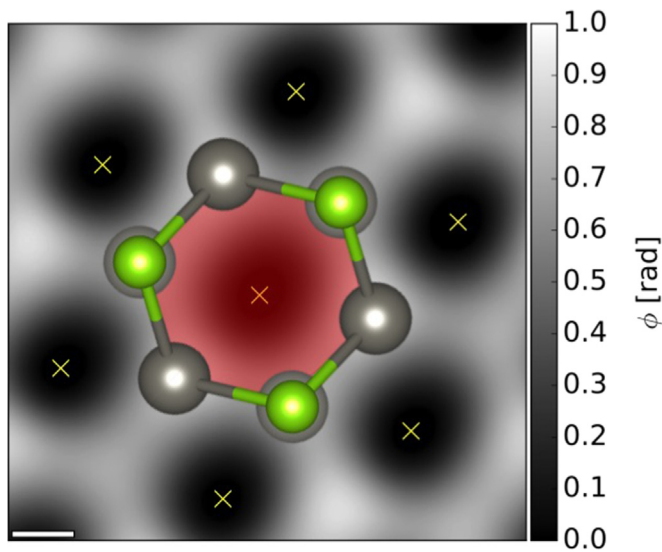


**Fig. 3.** Schematic diagram illustrating the setup of Voronoi tessellation on a phase image of WSe<sub>2</sub>. Green and gray spheres represent Se and W atoms, respectively. The yellow crosses show the positions of local minima in phase. An example of a Voronoi cell corresponding to the central minimum is marked by a red hexagon. The scale bar is 1 Å. (For interpretation of the references to color in this figure legend, the reader is referred to the web version of this article.)

wavefunction obtained using off-axis electron holography. Influences of the imaging system of the microscope, such as lens aberrations and the modulation transfer function (MTF) of the detector, were therefore also included in the simulated electron wavefunctions. The measured residual aberrations  $C_5 = 10 \mu\text{m}$  and  $C_5 = -6.5 \text{ mm}$  were taken into account.

The resolution limiting effects of partial temporal and partial spatial coherence can be neglected for a  $C_5$ - and  $C_c$ -corrected FEG microscope. Here, the resolution of the microscope was limited by an isotropic image spread of 22 pm (rms) [33]. The effect of image spread is simulated by a convolution of the electron wavefunction with a Gaussian function of respective width. When aiming for quantitative analysis, the incoherent effects of reducing contrast transfer in TEM also have to be taken into account [34]. The effect of the detector MTF on the wavefunction determined from the sideband of a hologram can be described in the sideband frequency regime. Considering that the typical MTF of a scintillator-based CCD detector exhibits an approximately exponential decay with increasing spatial frequency, the beams in the sideband that are located at higher spatial frequencies experience stronger attenuation than beams that are located at lower spatial frequencies. This difference leads to an asymmetry in attenuation in each sideband. In order to include this asymmetry in the simulations, the measured MTF of the detector was shifted by an amount and direction that reflect the sideband shift in the experiment, before it was multiplied by the centered beams of the simulated wavefunction. An objective aperture of semi-angle 15 mrad was included in the calculations, representing the circular mask that was used in the reconstruction of the experimental electron holograms.

Additional simulations were performed using the Semper image processing package [35], in order to investigate the influence of specimen tilt direction from [001] on the average phase and amplitude of the zero beam. The unit cell of WSe<sub>2</sub> was sampled by  $256 \times 256$  pixels in the  $x$ - $y$  directions and divided into 256 slices in the  $z$ -direction, which corresponds to a slice thickness close to 5 pm. Absorption was modeled using a constant factor of 0.05 [36].

### 3. Results and discussion

A representative off-axis electron hologram of a few-layer-thick WSe<sub>2</sub> flake is shown in Fig. 4a. Part of this hologram is enlarged in Fig. 4c in order to reveal the holographic fringes, which are magnified further in the inset. The application of a circular mask of semi-angle 15 mrad to the sideband in the Fourier transform of the hologram is shown in Fig. 4b. The resulting phase and amplitude images are shown in Fig. 4d and e, respectively.

Several interesting features are immediately apparent in Fig. 4. First, the phase image reveals the presence of contamination layers much more clearly than the amplitude image. This observation can be explained by comparing the mean inner potential of amorphous C (9.09 V [17]) with the calculated value for WSe<sub>2</sub> (21.5 V). Hence, an amorphous C layer whose thickness is similar to that of the WSe<sub>2</sub> specimen can produce a significant additional phase shift. Second, the amplitude and phase images show that a band of WSe<sub>2</sub> close to the specimen edge is thinner than that in the interior of the specimen. Unfortunately, the phase also indicates that the majority of this region is covered by contamination and is not suitable for quantitative analysis. Third, the asymmetry of the sidebands in the power spectrum of the hologram shown in Fig. 4b suggests that there is a significant deviation from the exact zone axis orientation.

Off-axis electron holograms were recorded from more than ten different areas on four WSe<sub>2</sub> flakes of different specimen thickness. Only regions that appeared to be clean and defect-free were selected for detailed analysis. Fig. 5 shows the phase and amplitude images corresponding to such a region of Fig. 4 and the average values for each Voronoi cell. Instead of the average amplitude  $A_{\Omega}$ , we plot here  $-2\ln(A_{\Omega})$ , which is expected to be proportional to specimen thickness in the absence of dynamical diffraction [11]. The low contrast in Fig. 5b and d indicates that the specimen is of homogeneous thickness without obvious crystal defects or additional contamination layers. Phase and amplitude images of all other regions, before and after averaging in Voronoi cells, are presented in the Supporting Information.

#### 3.1. Specimen thickness

A prerequisite for the quantitative measurement of electrostatic potentials using off-axis electron holography is the unambiguous and reliable determination of specimen thickness.

Fig. 6 shows values of  $\phi_{\Omega}$  and  $-2\ln(A_{\Omega})$  from simulations plotted as a function of specimen tilt angle for different specimen thicknesses. The background to the diagram shows histograms of the corresponding experimentally measured values, binned by 0.01 rad and 0.01, respectively, where a bright color corresponds to a high number of counts and a dark color corresponds to a low number of counts. The same histograms are shown more conventionally on the right side of each graph, as well as in Appendix A.

Fig. 6a shows that, close to a zone axis orientation, a measurement of  $\phi_{\Omega}$  does not allow an unambiguous determination of specimen thickness for only 3–6 layers of WSe<sub>2</sub>. As expected, the influence of dynamical diffraction becomes weaker when the specimen is tilted away from the zone axis orientation. A specimen tilt angle of  $\geq 2^\circ$  is sufficient to separate  $\phi_{\Omega}$  clearly for 1–6 layers of WSe<sub>2</sub>. At the highest specimen tilt angles,  $\phi_{\Omega}$  increases linearly with thickness, indicating a more or less kinematic regime. If the specimen is thin enough, (i.e., monolayer or bilayer WSe<sub>2</sub>), then the phase is almost unaffected by specimen tilt. As the specimen tilt angle is unknown in the experimental measurements, the unambiguous attribution of specimen thickness to each of the bands in the histogram is impossible from phase values alone. Just as for the phase,  $-2\ln(A_{\Omega})$  alone cannot be used for an

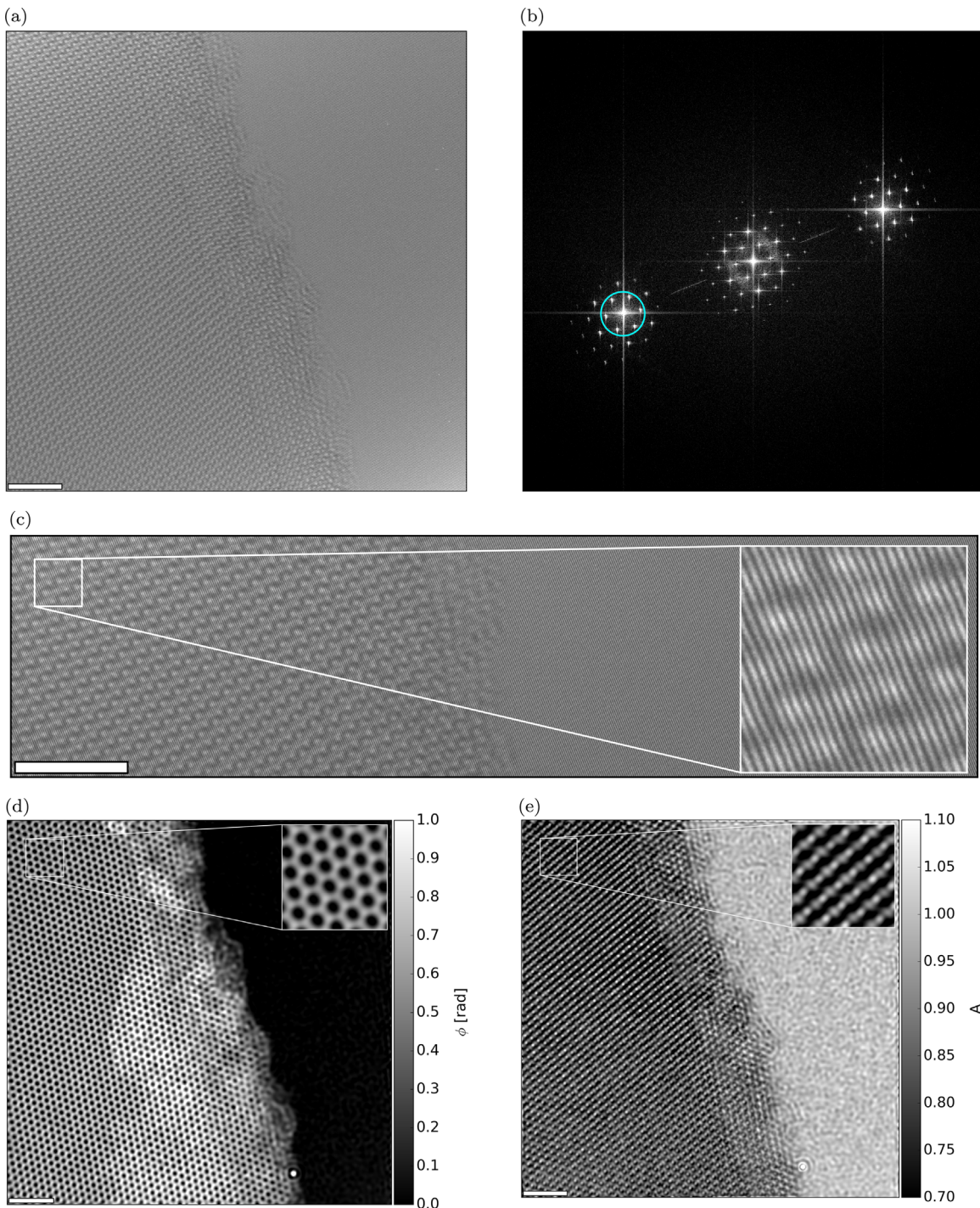


**Fig. 4.** (a) Off-axis electron hologram of a few-layer-thick WSe<sub>2</sub> crystal recorded at 80 kV, with a vacuum area on the right side. (b) Fourier transform of the hologram, with a circular mask of semi-angle 15 mrad marked around one of the sidebands by a circle. (c) Enlarged view of the top quarter of the hologram shown in Fig. 4a. The holographic fringes and their modulation due to the interaction with the atomic structure are visualized in the inset, which shows a small area at higher magnification. (d) Phase and (e) amplitude of the electron wavefunction reconstructed using the 15 mrad mask shown in Fig. 4b. The insets show magnified images of the marked areas. All scale bars are 2 nm.

unambiguous specimen thickness measurement in general. The main problem is the strong dependence of  $-2\ln(A_{\Omega})$  on specimen tilt angle for all values of specimen thickness above one monolayer of WSe<sub>2</sub>.

In order to make use of the opposing behavior of  $\phi_{\Omega}$  and  $-2\ln(A_{\Omega})$  with specimen tilt angle, we plotted experimental values of phase and  $-2\ln(A_{\Omega})$  together with simulated values in the form of a two-dimensional scatter plot of  $\phi_{\Omega}$  vs.  $-2\ln(A_{\Omega})$ . Fig. 7 shows the result, in which the simulated values are shown using colored

circles and experimental measurements are shown using small black dots, with each dot corresponding to a single Voronoi cell. Black lines connect simulated values that correspond to one specimen thickness. Cyan stars show the center of mass of each experimental data cloud. Each cloud may comprise data from several different areas of WSe<sub>2</sub>. Specifically, the bi-layer cloud comprises data from four different areas, the three-layer cloud and the two five-layer clouds each comprise data from only one area, while the four-layer and six-layer clouds each comprise data from two

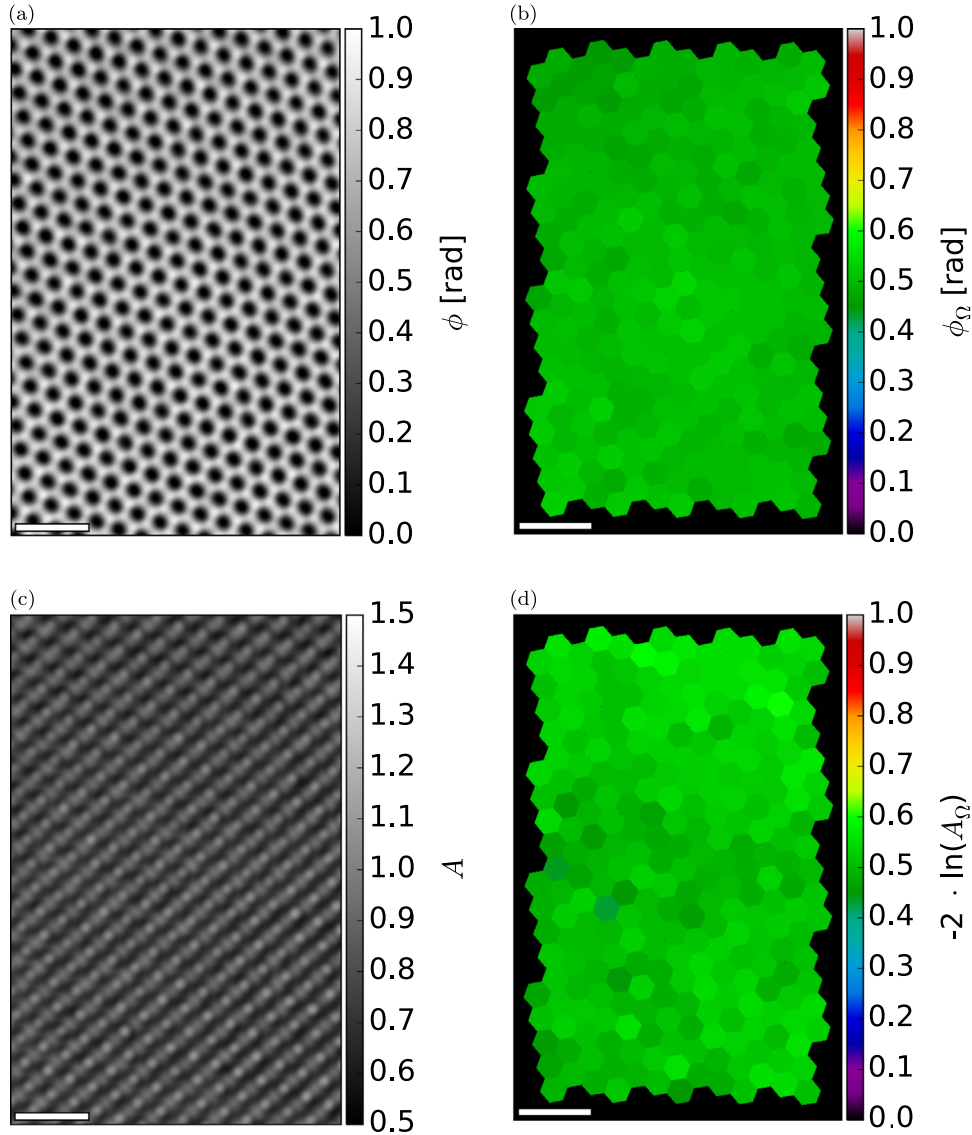


**Fig. 5.** (a) Phase  $\phi$  and (c) amplitude  $A$  images of the same region of a clean area of few-layer-thick  $\text{WSe}_2$  taken from the top left part of Fig. 4. (b) Phase  $\phi_\Omega$  and (d)  $-2 \ln(A_\Omega)$  after averaging within the area of each Voronoi cell  $\Omega$  constructed from the phase image in (a). The scale bars are 1 nm.

different areas. The standard deviation  $\sigma$  of the experimental data clouds was estimated from the root mean square of all individual standard deviations of all data clouds for  $\phi$  and  $-2 \ln(A)$  separately, yielding values of  $\sigma_\phi = 17$  mrad and  $\sigma_{-2 \ln(A)} = 0.024$ .

Although the experimental data clouds can now be matched closely to simulated values of both  $\phi_\Omega$  and  $-2 \ln(A_\Omega)$ , some of the clouds show phases that are smaller than those determined from the simulations. This discrepancy could originate either from a reduction in the elastic scattering potential due to bonding effects, which is expected to effectively reduce the phase by approximately 5–10%, or from the presence of defects such as vacancies in the crystal lattice.

The scatter plot shows that a reliable and unambiguous identification of specimen thickness is possible for few-layer-thick  $\text{WSe}_2$ . However, for a higher specimen thickness, such as five layers, the determination of specimen thickness can be ambiguous. The ambiguity is reduced at higher specimen tilt angles from a zone axis orientation. In addition to specimen thickness determination, Fig. 7 provides an estimate of specimen tilt angle.

Additional simulations of phase and amplitude performed using Semper were used to investigate whether the direction of specimen tilt angle from [001] should also be considered. Fig. 8a

shows the phase of the zero beam plotted as a function of specimen tilt angle and direction from [001] up to  $5^\circ$  for 1–6 layers of  $\text{WSe}_2$ . The simulations show that monolayer and bilayer  $\text{WSe}_2$  are almost unaffected by specimen tilt direction, which starts to be important for specimen thicknesses of at least six layers and larger tilt angles. In Fig. 8b, the average phase is plotted as a function of the specimen tilt direction from [001] for a specimen tilt angle of  $5^\circ$ . It can be seen that the direction of specimen tilt becomes more important for larger values of specimen thickness. Local variations for each line differ by a maximum of 13 mrad from the mean phase for a thickness of six layers. This is smaller than the average standard deviation in each of the clouds  $\sigma_\phi = 17$  mrad. Therefore, the direction of specimen tilt can be neglected in the present analysis. It may, however, be necessary to consider the direction of specimen tilt for other materials and for experiments involving larger magnitudes of tilt and specimen thickness.

### 3.2. Mean inner potential

As discussed above, for a specimen thickness of only one or two layers it is possible to apply the linear relationship between phase and electrostatic potential in Eqs. (2) and (3) in order to deduce

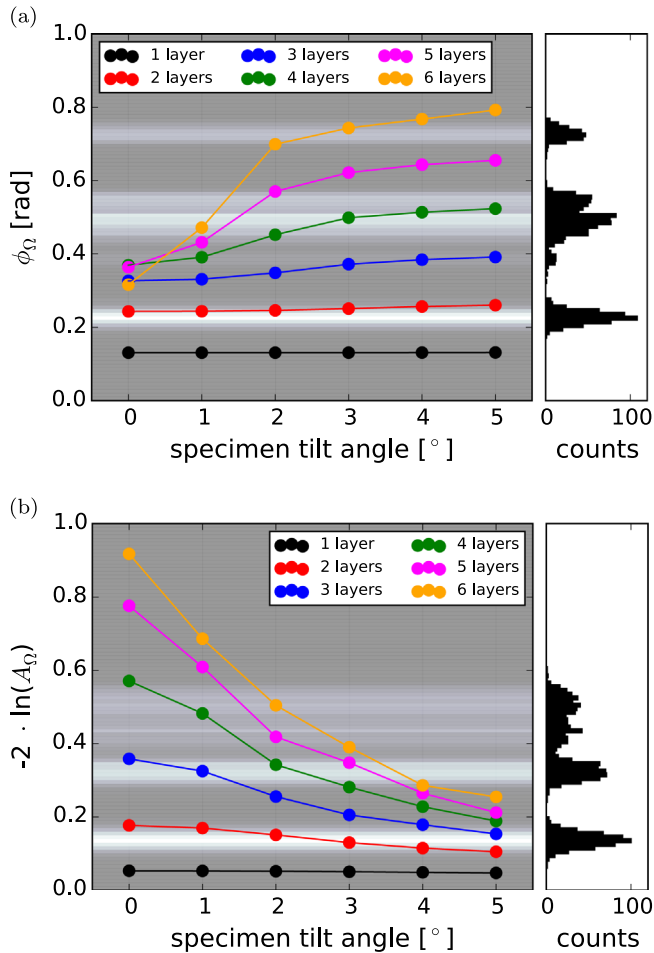


**Fig. 6.** Values of (a)  $\phi_{\Omega}$  and (b)  $-2\ln(A_{\Omega})$  obtained from simulations, plotted as a function of specimen tilt angle for different numbers of WSe<sub>2</sub> layers (i.e., different values of specimen thickness). The background in each plot shows a histogram (binning: 0.01 rad and 0.01, respectively) of corresponding experimentally measured values, where a bright color corresponds to a high number of counts and a dark color to a low number of counts. The experimental values are averaged over different specimen tilt angles. The histograms are shown more conventionally on the right side of each graph. (For interpretation of the references to color in this figure legend, the reader is referred to the web version of this article.)

the mean inner potential  $V_0$ .

In practice, the measurements of  $V_0$  can be complicated for a number of reasons, resulting from the requirement of very small specimen thickness, whereas the mean inner potential is in principle a bulk property [37–39]. Deviations between experiments performed for ultra-thin samples and calculated bulk properties may be caused by changes in electrostatic potential at the specimen surface, e.g. due to charge redistribution, changes in lattice parameters or surface reconstructions [17,20,37,40]. Although structural surface effects are expected to play a minor role in the case of WSe<sub>2</sub>, since it forms pristine surfaces without dangling bonds, for TMDs it is of interest in general to establish whether the mean inner potential depends on the number of layers. The presence of contamination layers on the WSe<sub>2</sub> surface can contribute significantly to the measured phase.

In order to determine the mean inner potential, linear regression was applied to the measured phase values of the data clouds corresponding to more than 2° tilt or less than three layers thickness, thereby minimizing the contribution of dynamical effects. This excludes only the two data sets corresponding to five layers in Fig. 7. The slope of the fitted line yields a value of  $\phi_{exp} = 124 \pm 5$  mrad, which represents the average phase shift per WSe<sub>2</sub> layer, as shown in Fig. B1. The relationship between phase and mean inner potential in Eq. (3) results in a value for  $V_0$  of  $18.9 \pm 0.8$  V. This value is approximately 12% lower than the value of 21.5 V calculated using neutral atomic scattering factors. The deviation is likely to be explained primarily by the fact that bonding effects are not included in the calculation, leading to an overestimate of  $V_0$  [11,20,23]. However, the measured phase shift may also be reduced by small remaining dynamical diffraction effects close to zone axis orientations. Such effects are very difficult to eliminate completely, in particular for samples as heavy as WSe<sub>2</sub> with thicknesses of more than one or two layers.

### 3.3. Mean free path

The present measurements can also be used to obtain insight into the use of electron holographic amplitude images to determine values of mean free path, which are typically found to lie in the range between 50 and 150 nm [37,41–44]. In general, the amplitude of the electron wavefunction depends on both elastic and inelastic scattering, according to Eq. (4). The total mean free

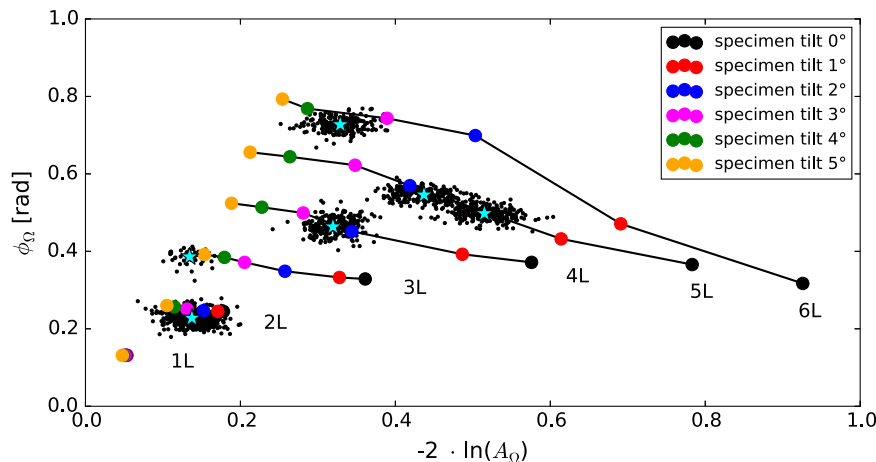


**Fig. 7.** Plot of phase shift  $\phi_{\Omega}$  vs  $-2\ln(A_{\Omega})$  extracted from experimental data by averaging in Voronoi cells corresponding to unit cells and simulated wavefunctions. The experimental data are in well-separated clouds and can therefore be assigned uniquely to different numbers of WSe<sub>2</sub> layers by taking into account specimen tilt angles of a few degrees. The simulated values are displayed by colored circles. Lines connect the points corresponding to the same thickness, labeled by number of layers (1L to 6L). The experimental data are plotted in the form of small black dots and the cyan colored stars display the center of mass of each cloud.

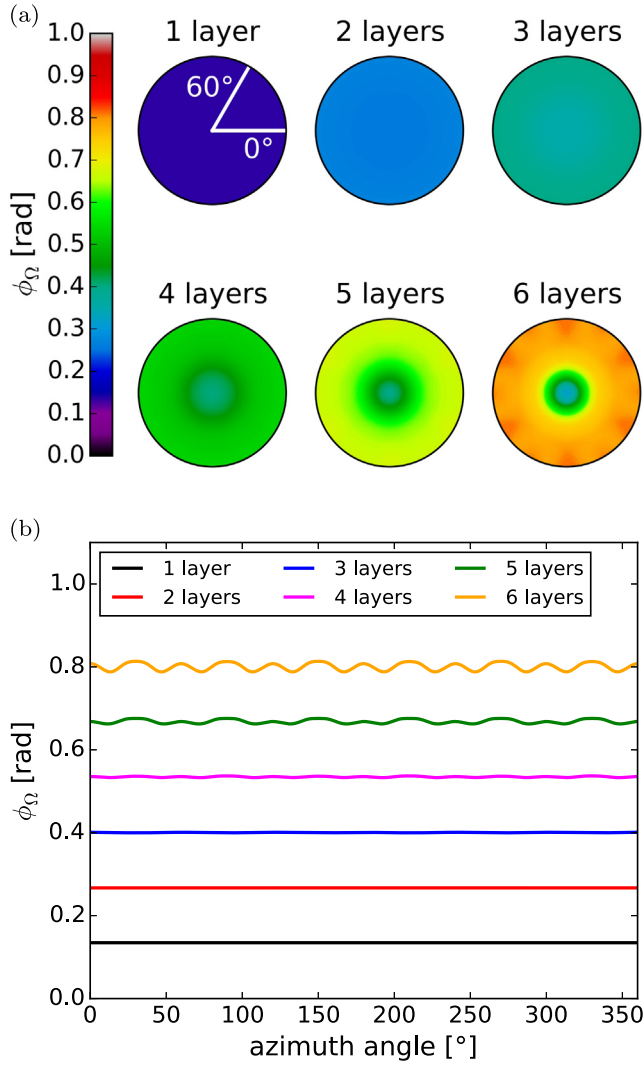


**Fig. 8.** (a) Simulated zero beam phase shift plotted as a function of tilt from [001] for one to six layers of WSe<sub>2</sub>. The tilt modulus ranges up to 5°. The tilt azimuth along 0° corresponds to the reciprocal [100] direction, while [010] is at 60° azimuth. (b) Phase shift of the zero beam for a tilt modulus of 5° plotted as a function of azimuth angle.

path for scattering (i.e., for electrons not contributing to the reconstructed amplitude image) can be written in the form

$$\frac{1}{\lambda_{tot}} = \frac{1}{\lambda_{in}} + \frac{1}{\lambda_{el}}, \quad (6)$$

where  $\lambda_{in}$  and  $\lambda_{el}$  correspond to the total inelastic mean free path and the mean free path for elastic scattering outside the mask of semi-angle  $\beta = 15$  mrad, respectively. Experimentally, the total mean free path  $\lambda_{tot}$  can be determined by making use of the linear relationship between  $-\ln(A_Q)$  and specimen thickness, according to Eq. (4). We selected the same data points as for the measurement of  $V_0$  and extracted a value for  $\lambda_{tot}$  from the slope of a linear fit of  $-\ln(A_Q)$  plotted as a function of specimen thickness, as shown in Fig. B2. This procedure yielded a total mean free path  $\lambda_{tot}$  of  $12 \pm 4$  nm. This value should be understood as a rough estimate, as there are only few data points available for the fit and the systematic dependence on specimen tilt angle has been neglected (see Fig. 6b). The total inelastic mean free path  $\lambda_{in}$  for WSe<sub>2</sub> can be predicted on the basis of scattering theory [45]. Assuming a collection semi-angle  $\beta$  of 15 mrad, the inelastic mean free path is

calculated to be  $\lambda_{in} = 51$  nm. The experimental value of  $\lambda_{tot}$  is much smaller than 51 nm, suggesting that the dominant scattering mechanism in the present experiments is elastic. This finding is further supported by the good match between the purely elastic simulations and the experimental amplitudes.

#### 4. Conclusions

The frequently applied approach of measuring electrostatic potentials from off-axis electron holograms is often based on the assumption of a direct linear relationship between the phase shift of the reconstructed wavefunction and specimen thickness. It relies on the assumption that dynamical effects, which result in a deviation from the linear relationship, can be neglected or minimized, for example by an appropriate choice of specimen orientation and thickness.

Here, we have studied the particular example of ultra-thin WSe<sub>2</sub> by recording high-resolution off-axis electron holograms at 80 kV close to the [001] zone axis, where dynamical diffraction effects can be strong. Computer simulations show that at an [001] zone axis orientation the linear relationship between phase and specimen thickness is only maintained sufficiently well for specimens containing one and two layers. This linear regime can be extended up to 6 layers when the specimen tilt angle is greater than 2° from [001]. However, the application of a few degrees of specimen tilt introduces additional uncertainties, as the measured phase depends on specimen tilt angle, which is rarely known independently. This problem can in principle be resolved by comparing both amplitudes and phases extracted from measurements with those obtained from computer simulations. A scatter plot in the complex plane then enables the determination of the specimen thickness with a precision of one WSe<sub>2</sub> layer with a spatial resolution of one projected unit cell, while also providing an estimate of the local specimen tilt. This approach could also serve as a starting point for a later detailed quantitative analysis of the lattice fringes in the same phase and amplitude images, for which aberrations and structural defects are likely to have a larger effect.

In the present study, the determination of specimen thickness and specimen tilt angle has been used to determine a value for the mean inner potential of WSe<sub>2</sub> of  $18.9 \pm 0.8$  V. Dynamical diffraction effects have been minimized by choosing specimen thicknesses of only one or two layers or specimen tilt angles of more than 2° from [001]. In comparison, the mean inner potential calculated directly from neutral atom scattering factors is 21.5 V. The two values differ by 12%, which is likely to result primarily from the influence of bonding, with a possible additional contribution from remaining dynamical diffraction effects.

A comparison of high-resolution electron holography data with simulations has been achieved on a quantitative level, enabling an assessment of the experimental conditions under which electrostatic potentials can be extracted from the phases of measured wavefunctions. Our approach enables the detection and potentially even a classification of adatoms, structural defects and charge redistribution in two-dimensional materials, for example at Schottky barriers and *p-n* junctions. The use of simulations that incorporate potentials obtained from ab initio calculations is likely to be required to fully explain values of the mean inner potential determined from experimental measurements for ultra-thin specimens of different thickness.

#### Acknowledgments

We are grateful to L. Houben, M. Lentzen, A. Thust, J. Caron and

C. B. Boothroyd for discussions, as well as A. Chaturvedi and C. Kloc from the School of Materials Science and Engineering, Nanyang Technological University, Singapore for providing the  $\text{WSe}_2$  crystals. The research leading to these results received funding from the German Science Foundation (DFG) under Grant MA 1280/40-1 and the European Research Council under the European Union's Seventh Framework Programme (FP7/2007–2013)/ ERC Grant agreement number 320832.

## Appendix A. Histograms

Fig. A1 and Fig. A2.

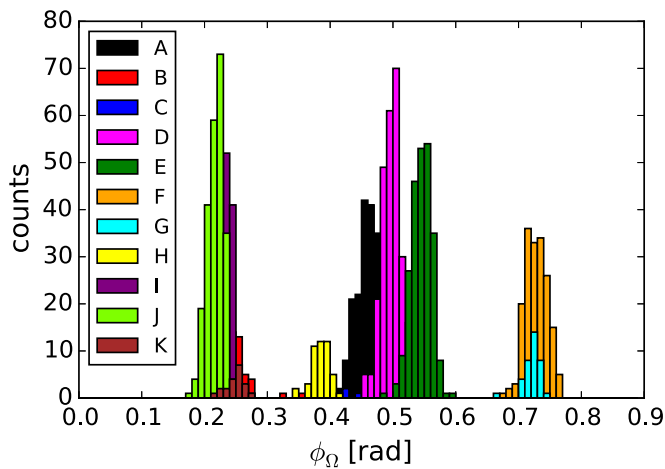


**Fig. A1.** Histogram of experimental phase measurements, with each color corresponding to a different analyzed phase image. The binning is 0.01 rad. (For interpretation of the references to color in this figure legend, the reader is referred to the web version of this article.)

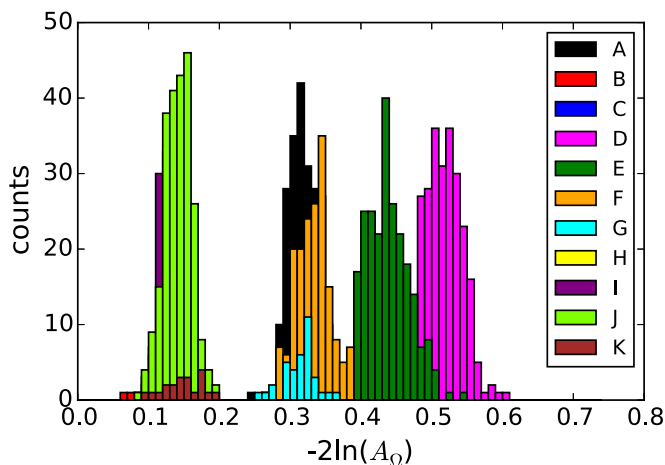


**Fig. A2.** Histogram of experimental  $-2\ln(A_\Omega)$  measurements, with each color corresponding to a different analyzed amplitude image. The binning is 0.01. (For interpretation of the references to color in this figure legend, the reader is referred to the web version of this article.)

## Appendix B. Linear fits to experimental data

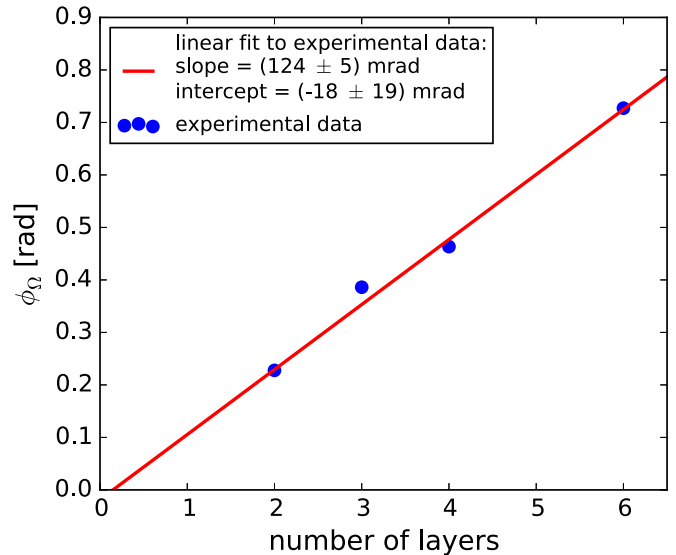


**Fig. B1.** Linear fit to experimental phase measurements plotted as a function of specimen thickness to obtain the average phase shift per  $\text{WSe}_2$  layer. The fitted parameters are shown in the legend as a slope and intercept. The error in each point, determined from the standard error in the mean, is too small to be visualized.

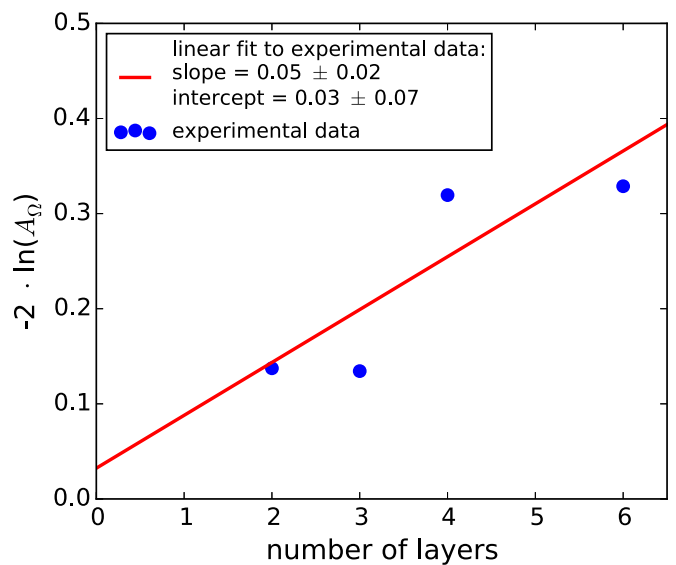


**Fig. B2.** Linear fit to experimental  $-2\ln(A_\Omega)$  measurements plotted as a function of specimen thickness to obtain the total mean free path  $\lambda_{tot}$ . The fitted parameters are displayed in the legend as a slope and intercept. The large scatter of the points is due to the strong dependence of the amplitude on specimen tilt.

## Appendix C. Supplementary data

Supplementary data associated with this article can be found in the online version at <http://dx.doi.org/10.1016/j.ultramic.2016.07.016>.

## References

- [1] W. Liu, J. Kang, D. Sarkar, Y. Khatami, D. Jena, K. Banerjee, Role of metal contacts in designing high-performance monolayer n-type  $\text{WSe}_2$  field effect transistors, *Nano Lett.* 13 (5) (2013) 1983–1990, <http://dx.doi.org/10.1021/nl304777e>.
- [2] W. Bao, X. Cai, D. Kim, K. Sridhara, M. Fuhrer, High mobility ambipolar  $\text{MoS}_2$

- field-effect transistors: substrate and dielectric effects, *Appl. Phys. Lett.* 102 (4) (2013) 042104, <http://dx.doi.org/10.1063/1.4789365>.
- [3] G. Lee, Y. Yu, X. Cui, N. Petrone, C. Lee, M. Choi, D. Lee, C. Lee, W. Yoo, K. Watanabe, T. Taniguchi, C. Nuckolls, P. Kim, J. Hone, Flexible and transparent MoS<sub>2</sub> field-effect transistors on hexagonal boron nitride-graphene heterostructures, *ACS Nano* 7 (9) (2013) 7931–7936, <http://dx.doi.org/10.1021/nn402954e>.
- [4] P. Tonndorf, R. Schmidt, P. Böttger, X. Zhang, J. Börner, A. Liebig, M. Albrecht, C. Kloc, O. Gordan, D. Zahn, S. Michaelis de Vasconcellos, R. Bratschitsch, Photoluminescence emission and raman response of monolayer MoS<sub>2</sub>, MoSe<sub>2</sub> and WSe<sub>2</sub>, *Opt. Express* 21 (4) (2013) 4908–4916, <http://dx.doi.org/10.1364/OE.21.004908>, URL <http://www.opticsexpress.org/abstract.cfm?URI=oe-21-4-4908>.
- [5] Z. Zhu, Y. Cheng, U. Schwingenschlögl, Giant spin-orbit-induced spin splitting in two-dimensional transition-metal dichalcogenide semiconductors, *Phys. Rev. B* 84 (2011) 153402, <http://dx.doi.org/10.1103/PhysRevB.84.153402>, URL <http://link.aps.org/doi/10.1103/PhysRevB.84.153402>.
- [6] K. Kośmider, J.W. González, J. Fernández-Rossier, Large spin splitting in the conduction band of transition metal dichalcogenide monolayers, *Phys. Rev. B* 88 (2013) 245436, <http://dx.doi.org/10.1103/PhysRevB.88.245436>, URL <http://link.aps.org/doi/10.1103/PhysRevB.88.245436>.
- [7] D. Cooper, C. Ailliot, J.-P. Barnes, J.-M. Hartmann, P. Salles, G. Benassyag, R. E. Dunin-Borkowski, Dopant profiling of focused ion beam milled semiconductors using off-axis electron holography; reducing artifacts, extending detection limits and reducing the effects of gallium implantation, *Ultramicroscopy* 110 (5) (2010) 383–389, <http://dx.doi.org/10.1016/j.ultramicro.2010.02.001>, URL <http://www.sciencedirect.com/science/article/pii/S0304399110000288>.
- [8] S. Yazdi, T. Kasama, M. Beleggia, M.S. Yekta, D.W. McComb, A.C. Twitche-Harrison, R.E. Dunin-Borkowski, Towards quantitative electrostatic potential mapping of working semiconductor devices using off-axis electron holography, *Ultramicroscopy* 152 (2015) 10–20, <http://dx.doi.org/10.1016/j.ultramicro.2014.12.012>, URL <http://www.sciencedirect.com/science/article/pii/S0304399114002691>.
- [9] M.R. McCartney, N. Agarwal, S. Chung, D.A. Cullen, M.-G. Han, K. He, L. Li, H. Wang, L. Zhou, D.J. Smith, Quantitative phase imaging of nanoscale electrostatic and magnetic fields using off-axis electron holography, *Ultramicroscopy* 110 (5) (2010) 375–382, <http://dx.doi.org/10.1016/j.ultramicro.2010.01.001>, URL <http://www.sciencedirect.com/science/article/pii/S0304399110000045>.
- [10] H. Lichte, P. Formanek, A. Lenk, M. Linck, C. Matzeck, M. Lehmann, P. Simon, Electron holography: applications to materials questions, *Annu. Rev. Mater. Res.* 37 (1) (2007) 539–588, <http://dx.doi.org/10.1146/annurev.matsci.37.052506.084232>.
- [11] R.E. Dunin-Borkowski, M.R. McCartney, D.J. Smith, Electron holography of nanostructured materials, in: H. Nalwa (Ed.), *Encyclopedia of Nanoscience and Nanotechnology*, 3, American Scientific Publishers, USA, 2004, pp. 41–100.
- [12] A. Lubk, D. Wolf, F. Kern, F. Röder, P. Prete, N. Lovergine, H. Lichte, Nanoscale three-dimensional reconstruction of elastic and inelastic mean free path lengths by electron holographic tomography, *Appl. Phys. Lett.* 105 (17) (2014) 042104, <http://dx.doi.org/10.1063/1.4900406>.
- [13] A. Lubk, D. Wolf, P. Prete, N. Lovergine, T. Niermann, S. Sturm, H. Lichte, Nanometer-scale tomographic reconstruction of three-dimensional electrostatic potentials in GaAs/AlGaAs core-shell nanowires, *Phys. Rev. B* 90 (2014) 125404, <http://dx.doi.org/10.1103/PhysRevB.90.125404>.
- [14] W. Schutte, J.D. Boer, F. Jellinek, Crystal structures of tungsten disulfide and diselenide, *J. Solid State Chem.* 70 (2) (1987) 207–209, [http://dx.doi.org/10.1016/0022-4596\(87\)90057-0](http://dx.doi.org/10.1016/0022-4596(87)90057-0), URL <http://www.sciencedirect.com/science/article/pii/0022459687900570>.
- [15] Visualization for Electronic and Structural Analysis (Vesta) (2015). URL <http://jp-minerals.org/vesta/en/>.
- [16] R. Zan, Q.M. Ramasse, R. Jalil, T. Georgiou, U. Bangert, K.S. Novoselov, Control of radiation damage in MoS<sub>2</sub> by graphene encapsulation, *ACS Nano* 7 (11) (2013) 10167–10174, <http://dx.doi.org/10.1021/nn4044035>, PMID: 24116975.
- [17] M. Wanner, D. Bach, D. Gerthsen, R. Werner, B. Tesche, Electron holography of thin amorphous carbon films: measurement of the mean inner potential and a thickness-independent phase shift, *Ultramicroscopy* 106 (4–5) (2006) 341–345, <http://dx.doi.org/10.1016/j.ultramicro.2005.10.004>, URL <http://www.sciencedirect.com/science/article/pii/S0304399105002305>.
- [18] M. Gajdardziska-Josifovska, M. McCartney, W. de Ruijter, D.J. Smith, J. Weiss, J. Zuo, Accurate measurements of mean inner potential of crystal wedges using digital electron holograms, *Ultramicroscopy* 50 (3) (1993) 285–299, [http://dx.doi.org/10.1016/0304-3991\(93\)90197-6](http://dx.doi.org/10.1016/0304-3991(93)90197-6), URL <http://www.sciencedirect.com/science/article/pii/0304399193901976>.
- [19] D. Rez, P. Rez, I. Grant, Dirac-Fock calculations of X-ray scattering factors and contributions to the mean inner potential for electron scattering, *Acta Crystallogr. Sect. A* 50 (4) (1994) 481–497, <http://dx.doi.org/10.1107/S0108767393013200>.
- [20] P. Kruse, A. Rosenauer, D. Gerthsen, Determination of the mean inner potential in III–V semiconductors by electron holography, *Ultramicroscopy* 96 (1) (2003) 11–16, [http://dx.doi.org/10.1016/S0304-3991\(02\)00376-5](http://dx.doi.org/10.1016/S0304-3991(02)00376-5), URL <http://www.sciencedirect.com/science/article/pii/S0304399102003765>.
- [21] D. Saldin, J. Spence, On the mean inner potential in high- and low-energy electron diffraction, *Ultramicroscopy* 55 (4) (1994) 397–406, [http://dx.doi.org/10.1016/0304-3991\(94\)90175-9](http://dx.doi.org/10.1016/0304-3991(94)90175-9), URL <http://www.sciencedirect.com/science/article/pii/0304399194901759>.
- [22] M. O’Keefe, J.C.H. Spence, On the average Coulomb potential ( $\Sigma_0$ ) and constraints on the electron density in crystals, *Acta Crystallogr. Sect. A* 50 (1) (1994) 33–45, <http://dx.doi.org/10.1107/S010876739300474X>.
- [23] R.S. Pennington, C.B. Boothroyd, R.E. Dunin-Borkowski, Surface effects on mean inner potentials studied using density functional theory, *Ultramicroscopy* 159 (2015) 34–45, <http://dx.doi.org/10.1016/j.ultramicro.2015.07.011>, URL <http://www.sciencedirect.com/science/article/pii/S0304399115300176>.
- [24] A. Castellanos-Gomez, M. Buscema, R. Molenaar, V. Singh, L. Janssen, H. van der Zant, G. Steele, Deterministic transfer of two-dimensional materials by dry viscoelastic stamping, *2D Mater.* 1 (1) (2014) 011002, URL <http://stacks.iop.org/2053-1583/1/i=1/a=011002>.
- [25] J. Barthel, L. Houben, K. Tillmann, Fei titan G3 50–300 PICO, J. Large-Scale Res. Facil. 1 (2015) A34, <http://dx.doi.org/10.17815/jlsrf-1-57>, URL <http://nbn-resolving.org/urn:nbn:de:0001-jlsrf-1-57-4>.
- [26] E. Völk, L.F. Allard, D.C. Joy, Introduction to Electron Holography, Springer, New York, 1999, URL <http://link.springer.com/book/10.1007%2F978-1-4615-4817-1>.
- [27] M. Linck, Optimum aberration coefficients for recording high-resolution off-axis holograms in a Cs-corrected {TEM}, *Ultramicroscopy* 124 (2013) 77–87, <http://dx.doi.org/10.1016/j.ultramicro.2012.08.006>, URL <http://www.sciencedirect.com/science/article/pii/S0304399112002100>.
- [28] A. Rosenauer, T. Mehrtens, K. Müller, K. Gries, M. Schowalter, P.V. Satyam, S. Bley, C. Tessarek, D. Hommel, K. Sebal, M. Seyfried, J. Gutowski, A. Avramescu, K. Engl, S. Lutgen, Composition mapping in gan by scanning transmission electron microscopy, *Ultramicroscopy* 111 (8) (2011) 1316–1327, <http://dx.doi.org/10.1016/j.ultramicro.2011.04.009>, URL <http://www.sciencedirect.com/science/article/pii/S0304399111001598>.
- [29] J.M. Cowley, A.F. Moodie, The scattering of electrons by atoms and crystals I. A new theoretical approach, *Acta Crystallogr.* 10 (10) (1957) 609–619, <http://dx.doi.org/10.1107/S0365110X57002194>.
- [30] J. Barthel, Dr. probe - high-resolution (s)tem image simulation software (2015). URL <http://www.er-c.org/barthel/drprobe/>.
- [31] F.Z. Chien, Y.S. Chen, Y.C. Chu, W.Y. You, J.B. Lee, T.E. Dann, C.H. Tu, Y.S. Huang, An X-ray measurement of Debye Waller factors of single crystal MoSe<sub>2</sub> and WSe<sub>2</sub>, *Chin. J. Phys.* 26 (1988) 119.
- [32] A. Weickenmeier, H. Kohl, Computation of absorptive form factors for high-energy electron diffraction, *Acta Crystallogr. Sect. A* 47 (5) (1991) 590–597, <http://dx.doi.org/10.1107/S0108767391004804>.
- [33] M. Haider, P. Hartel, H. Müller, S. Uhlemann, J. Zach, Information transfer in a tem corrected for spherical and chromatic aberration, *Microsc. Microanal.* 16 (2010) 393–408, <http://dx.doi.org/10.1017/S1431927610013498>.
- [34] C.L. Jia, S.B. Mi, J. Barthel, D.W. Wang, R.E. Dunin-Borkowski, K.W. Urban, A. Thust, Determination of the 3d shape of a nanoscale crystal with atomic resolution from a single image, *Nat. Mater.* 13 (11) (2014) 1044–1049, <http://dx.doi.org/10.1038/nmat4087> (article).
- [35] W. Saxton, T. Pitt, M. Horner, Digital image processing: the Semper system, *Ultramicroscopy* 4 (3) (1979) 343–353, [http://dx.doi.org/10.1016/S0304-3991\(79\)80044-3](http://dx.doi.org/10.1016/S0304-3991(79)80044-3), URL <http://www.sciencedirect.com/science/article/pii/S0304399179800443>.
- [36] H. Hashimoto, A. Howie, M.J. Whelan, Anomalous electron absorption effects in metal foils: Theory and comparison with experiment, *Proc. R. Soc. Lond. Ser. A Math. Phys. Sci.* 269 (1336) (1962) 80–103.
- [37] S. Chung, D.J. Smith, M.R. McCartney, Determination of the inelastic mean-free-path and mean inner potential for AlAs and GaAs using off-axis electron holography and convergent beam electron diffraction, *Microsc. Microanal.* 13 (2007) 329–335, <http://dx.doi.org/10.1017/S1431927607070687>, URL [http://journals.cambridge.org/article\\_S1431927607070687](http://journals.cambridge.org/article_S1431927607070687).
- [38] K. Yada, K. Shibata, T. Hibi, A high resolution electron interference microscope and its application to the measurement of mean inner potential, *J. Electron Microsc.* 22 (3) (1973) 223–230, arXiv <http://jmicro.oxfordjournals.org/content/22/3/223.full.pdf+html>.
- [39] J. Li, M.R. McCartney, R.E. Dunin-Borkowski, D.J. Smith, Determination of mean inner potential of germanium using off-axis electron holography, *Acta Crystallogr. Sect. A* 55 (4) (1999) 652–658, <http://dx.doi.org/10.1107/S010876739801719X>.
- [40] R. Popescu, E. Müller, M. Wanner, D. Gerthsen, M. Schowalter, A. Rosenauer, A. Böttcher, D. Löffler, P. Weis, Increase of the mean inner coulomb potential in Au clusters induced by surface tension and its implication for electron scattering, *Phys. Rev. B* 76 (2007) 235411, <http://dx.doi.org/10.1103/PhysRevB.76.235411>.
- [41] M. McCartney, M. Gajdardziska-Josifovska, Absolute measurement of normalized thickness,  $t/\lambda_i$ , from off-axis electron holography, *Ultramicroscopy* 53 (3) (1994) 283–289, [http://dx.doi.org/10.1016/0304-3991\(94\)90040-X](http://dx.doi.org/10.1016/0304-3991(94)90040-X).
- [42] A. Lubk, D. Wolf, H. Lichte, The effect of dynamical scattering in off-axis holographic mean inner potential and inelastic mean free path measurements, *Ultramicroscopy* 110 (5) (2010) 438–446, <http://dx.doi.org/10.1016/j.ultramicro.2009.09.009>, URL <http://www.sciencedirect.com/science/article/pii/S0304399109002058>.
- [43] K. Iakoubovskii, K. Mitsuishi, Y. Nakayama, K. Furuya, Mean free path of inelastic electron scattering in elemental solids and oxides using transmission electron microscopy: atomic number dependent oscillatory behavior, *Phys. Rev. B* 77 (2008) 104102, <http://dx.doi.org/10.1103/PhysRevB.77.104102>.
- [44] T. Chou, M. Libera, Mean free paths for inelastic electron scattering in silicon and poly(styrene) nanospheres, *Ultramicroscopy* 94 (1) (2003) 31–35, [http://dx.doi.org/10.1016/S0304-3991\(02\)00192-4](http://dx.doi.org/10.1016/S0304-3991(02)00192-4).
- [45] R. Egerton, *Electron Energy-Loss Spectroscopy in the Electron Microscope*, Springer, US, 2011, URL <http://www.springer.com/de/book/9781441995827>.